

Electronic structure and magnetic breakdown in titanium

O. Jepsen

AEK Research Establishment, Risø, Roskilde, Denmark

(Received 7 July 1975)

Using the linear muffin-tin-orbital method, we have calculated the electronic structure of the $3d$ hcp transition-metal Ti. Our Fermi surface is in good agreement with the recent de Haas-van Alphen experiments of Kamm and Anderson, and a quantitative comparison indicates that the calculated d band lies less than about 10 mRy too high relative to the sp bands. Magnetic breakdown plays an essential part in the interpretation of the experimental results. We also compare our results with previous calculations on Ti.

I. INTRODUCTION

After scandium, titanium is the transition metal with the lowest atomic number ($Z = 22$) and like the other two group-IV elements Zr and Hf it crystallizes in the hexagonal-close-packed (hcp) structure. The close similarity of the Fermi surfaces and the electronic structures of the $4d$ and $5d$ elements in the same column of the periodic table has been established through a number of experiments and calculations^{1,4} but, owing to the magnetism of the heavier $3d$ metals, the comparison has not generally been extended to these. The lighter $3d$ metals Sc, Ti, and V are nonmagnetic and the recent de Haas-van Alphen (dHvA) results of Kamm and Anderson² and Everett³ indicate that the Fermi surfaces of Ti and Zr are quite similar. However, a comparison between the recent band-structure calculations of Jepsen, Andersen, and Mackintosh⁴ (hereafter referred to as JAM) for Zr and Hf with the calculations of Hygh and Welch^{5,6,7} on Ti seems to indicate that the similarity between the $4d$ Zr and the $5d$ Hf does not extend to the $3d$ Ti. On the other hand, Hygh and Welch found that the Ti bands were very sensitive to small modifications of the potential, so we decided to recalculate the electronic structure of Ti by exactly the same procedure as that of JAM, i. e., using a muffin-tin potential constructed from overlapping relativistic charge densities, with the Slater $\rho^{1/3}$ approximation for the exchange and correlation, and employing the linear muffin-tin-orbital (MTO) method of Andersen¹¹ for the evaluation of the eigenvalues. This approach should be equivalent to that of Hygh and Welch^{5,7} except that we have included all relativistic effects throughout the calculation, but, contrary to their results, we find an electronic structure which is in good agreement with the experimental Fermi surface² and which is closely similar to those of the other group-IV elements.

A number of calculations have been made on Ti,⁵⁻¹⁰ but none of these can adequately describe the dHvA frequencies recently observed by Kamm

and Anderson.² Altmann and Cohan⁸ have tested three potentials by calculating the eigenvalues at $\vec{k} = \vec{0}$ using the cellular method. The three sets of eigenvalues differ from each other and from our values by as much as several tenths of a rydberg. A preliminary energy-band calculation has been presented by Mattheiss⁹ using the augmented-plane-wave (APW) method. He calculated the bands along the line from Γ to K in the Brillouin zone (see Fig. 1) and they are in fair agreement with our results. The discrepancies, of the order of 50 mRy, are due to small differences in the potentials and the neglect of relativistic effects in the calculation by Mattheiss. The first theoretical calculation of the Fermi surface of Ti was carried out by Altmann and Bradley¹⁰ using a modified form of the cellular method with three potentials based on Hartree-Fock calculations for the Ti^{+2} , Ti^{+3} , and Ti^{+4} ions and a uniform charge distribution of one, two, and three electrons per atom, respectively. The bands so obtained show a general similarity to our results, but there are a large number of differences of detail. The three papers of Hygh and Welch⁵⁻⁷ [hereafter referred to as HW(I),⁵ WH(II),⁶ and WH(III)⁷] present the energy bands and Fermi surfaces resulting from APW calculations, with Mattheiss's¹² construction for the muffin-tin (MT) potential. HW(I) and WH(III) used the configurations s^2 and s^1 in the atomic calculations, respectively, and full Slater exchange ($\alpha = 1$), while WH(II) performed a self-consistent calculation starting with the potential of HW(I), but with the core orbitals "frozen" and the exchange parameter $\alpha = \frac{3}{4}$. The results of these three calculations are very similar, but they all differ substantially from what we find.

The organization of the present paper is as follows. In Sec. II we briefly describe the linear MTO method and some details of the calculations. In Sec. III we present the results of the calculations, which include energy bands, density of states, Fermi-surface cross sections, and the cyclotron masses. These are then compared with

experiments and results of previous calculations on Ti, Zr, and Hf.

II. METHOD OF CALCULATION

The linear MTO method has been discussed in detail by Andersen¹¹ and an abbreviated descrip-

tion of its concepts has been given by JAM. We shall therefore comment only on those aspects which are particularly relevant to this calculation.

In the neighborhood of the arbitrary energy E_ν , the Hamiltonian and overlap matrices in the lmq representation and in the atomic-sphere approximation (ASA)¹³ are

$$H_{l'm'q',lmq}^{\vec{k}} \equiv \langle \chi_{l'm'q'}^{\vec{k}} | H - E_\nu | \chi_{lmq}^{\vec{k}} \rangle = \omega_l(-l-1)\delta_{l'l'}\delta_{m'm}\delta_{q'q} - \left(1 + \frac{\omega_{l'}(l')}{\omega_{l'}(-l'-1) - \omega_{l'}(l')} + \frac{\omega_l(l)}{\omega_l(-l-1) - \omega_l(l)}\right) T_{l'm'q',lmq}^{\vec{k}} + \sum_{\lambda\mu\rho} T_{l'm'q',\lambda\mu\rho}^{\vec{k}} \frac{\omega_\lambda(\lambda)}{[\omega_\lambda(-\lambda-1) - \omega_\lambda(\lambda)]^2} T_{\lambda\mu\rho,lmq}^{\vec{k}} \quad (1)$$

and

$$O_{l'm'q',lmq}^{\vec{k}} \equiv \langle \chi_{l'm'q'}^{\vec{k}} | \chi_{lmq}^{\vec{k}} \rangle = [1 + \langle \dot{\phi}_{\nu l}^2 \rangle \omega_l^2(-l-1)] \delta_{l'l'}\delta_{m'm}\delta_{q'q} - \left(\frac{1 + \langle \dot{\phi}_{\nu l'}^2 \rangle \omega_{l'}(-l'-1)\omega_{l'}(l')}{\omega_{l'}(-l'-1) - \omega_{l'}(l')} + \frac{1 + \langle \dot{\phi}_{\nu l}^2 \rangle \omega_l(-l-1)\omega_l(l)}{\omega_l(-l-1) - \omega_l(l)} \right) T_{l'm'q',lmq}^{\vec{k}} + \sum_{\lambda\mu\rho} T_{l'm'q',\lambda\mu\rho}^{\vec{k}} \frac{1 + \langle \dot{\phi}_{\nu \lambda}^2 \rangle \omega_\lambda^2(\lambda)}{[\omega_\lambda(-\lambda-1) - \omega_\lambda(\lambda)]^2} T_{\lambda\mu\rho,lmq}^{\vec{k}}, \quad (2)$$

with

$$T_{l'm'q',lmq}^{\vec{k}} \equiv \sqrt{\frac{1}{2}S} \Phi_{l'}(-l'-1) \delta_{l'm'q',lmq}^{\vec{k}} \sqrt{\frac{1}{2}S} \Phi_l(-l-1),$$

where lm are the angular momentum quantum numbers, and q is the site index.

The canonical structure constants are given by the lattice sums

$$S_{l'm'q',lmq}^{\vec{k}} = g_{l'm'q',lm} \sum_{\vec{R} \neq \vec{0}} e^{i\vec{k} \cdot \vec{R}} \frac{S^{\lambda+1}}{|\vec{R} - \vec{\rho}|^{\lambda+1}} \times \left[\sqrt{4\pi} i^\lambda Y_{\lambda\mu} \left(\frac{\vec{R} - \vec{\rho}}{|\vec{R} - \vec{\rho}|} \right) \right]^*$$

where g is a coefficient given by Andersen,¹¹ the atomic sphere radius is $S = \frac{1}{2}(3\Omega/\pi)^{1/3}$, and $\vec{\rho} \equiv \vec{q}' - \vec{q}$, $\lambda \equiv l' + l$, and $\mu \equiv m' - m$.

The energies $\omega_l(-l-1)$, $\omega_l(l)$, $S\Phi_l^2(-l-1)$ and $\langle \dot{\phi}_{\nu l}^2 \rangle^{-1/2}$ are potential parameters that may be obtained by fitting the logarithmic derivative function $D_l(E) \equiv S\phi_l'(E, S)/\phi_l(E, S)$ at the atomic sphere to the Laurent series

$$\frac{1}{D_l(E) - D_{\nu l}} = -\frac{1}{m_{\nu l}(E - E_\nu)} + a_{\nu l} + (E - E_\nu) b_{\nu l}$$

and using

$$\omega_l(D) = \frac{1}{m_{\nu l}} \frac{1}{a_{\nu l} + (D_{\nu l} - D)^{-1}}$$

and

$$S\Phi_l^2(D) = \frac{1}{m_{\nu l}} \left(\frac{1}{1 + (D_{\nu l} - D)a_{\nu l}} \right)^2,$$

with $D = l$ or $D = -l - 1$. Moreover

$$\langle \dot{\phi}_{\nu l}^2 \rangle = m_{\nu l} b_{\nu l}$$

If we neglect the structure constants with $l' \neq l$, it may be shown that (1) and (2) yield the unhybridized energy bands

$$E(D_{ii}^{\vec{k}}) = E_\nu + \frac{\omega_l(D_{ii}^{\vec{k}})}{1 + \langle \dot{\phi}_{\nu l}^2 \rangle \omega_l^2(D_{ii}^{\vec{k}})},$$

where

$$\omega_l(D_{ii}^{\vec{k}}) = \omega_l(-l-1) + \frac{1}{2}S\Phi_l^2(-l-1) \frac{S_{ii}^{\vec{k}}}{1 - \gamma_l S_{ii}^{\vec{k}}}$$

and

$$\gamma_l \equiv \frac{\Phi_l(-l-1)}{2(2l+1)\Phi_l(l)} = \frac{\frac{1}{2}S\Phi_l^2(-l-1)}{\omega_l(-l-1) - \omega_l(l)} = \frac{1}{4l+2} \frac{1 + (D_{\nu l} - l)a_{\nu l}}{1 + (D_{\nu l} + l + 1)a_{\nu l}}.$$

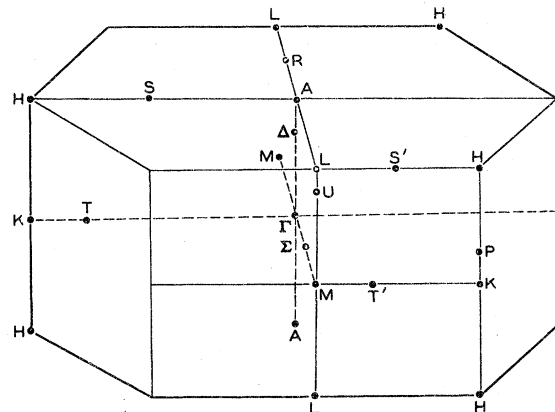


FIG. 1. Brillouin zone for the hexagonal structure.

The canonical l bands,

$$s_{ii}^k = 2(2l+1)(D_{ii}^k + l + 1)/(D_{ii}^k - l),$$

are the eigenvalues of the ll subblock $s_{im', q', imq}^k$ of the structure-constant matrix. We may then conclude that the unhybridized νl -energy-band structure is derived from the canonical l -band structure by fixing the band position through

$$E(-l-1) = E_\nu + \frac{\omega(-l-1)}{1 + \langle \dot{\phi}_\nu^2 \rangle \omega^2(-l-1)},$$

scaling it by

$$\frac{1}{\mu S^2} \equiv \frac{1}{2} S \Phi^2(-l-1) \frac{1 - \langle \dot{\phi}_\nu^2 \rangle \omega^2(-l-1)}{[1 + \langle \dot{\phi}_\nu^2 \rangle \omega^2(-l-1)]^2},$$

and distorting it nonlinearly by $\Phi(-l-1)/\Phi(l)$ and $\langle \dot{\phi}_\nu^2 \rangle$. In these equations we have dropped the subscript l . The band position, $E(-l-1)$, corresponds to the center of gravity of the canonical l band and the parameter μ is unity for free electrons so that it is the intrinsic band mass. For transition-metal d bands $\Phi(-l-1)/\Phi(l)$ is much less than unity, so that the width of the d band is approximately $25/\mu_d S^2 \approx 12.5 S \Phi_d^2(-3)$. When comparing the bands of metals with different lattice constants it is most convenient to use the dimensionless parameters

$$C_{l', l} \equiv [E_{l'}(-l'-1) - E_l(-l-1)] S^2$$

and $\mu_{l'}$.

In the present calculation we included in (1) and (2) the correction to the ASA, plus the relativistic effects, by the technique described by Andersen.¹¹ The correction introduces the potential parameter V_{MTZ} , which is the muffin-tin zero, and the spin-orbit coupling introduces the two potential param-

eters $\xi_l(D_{\nu l})$ and $\omega_l(D_l^T)$, in terms of which the spin-orbit coupling parameter at logarithmic derivative D is given by

$$\xi(D) = \xi(D_\nu) \left(1 - \frac{\omega(D)}{\omega(D^T)}\right)^2 / [1 + \langle \dot{\phi}_\nu^2 \rangle \omega^2(D)],$$

and where we have again dropped the subscript l . The relativistic mass-velocity and Darwin effects are included in the potential parameters $\omega(-l-1)$, $S \Phi^2(-l-1)$, $\Phi(-l-1)/\Phi(l)$, and $\langle \dot{\phi}_\nu^2 \rangle$.

In the present calculation we have used the full linear MTO formalism including s , p , and d MTOs, which for the hcp structure with two atoms per primitive cell, including spin-orbit coupling, results in Hamiltonian and overlap matrices of dimension 36×36 .

We have used the hcp structure constants throughout the Brillouin zone calculated by JAM, corresponding to a c/a ratio of 1.58, although the room-temperature lattice constants of Ti ($a = 5.5754$ a.u. and $c = 8.8502$ a.u.) correspond to a c/a ratio of 1.5873.¹⁴ The rms deviation of the energies for these two c/a ratios and the same atomic volume (the atomic radius $S = 3.0524$ a.u.) calculated for the lowest ten bands at 84 \vec{k} points along the symmetry lines was 1 mRy. The correct c/a ratio was used for the energy bands of Fig. 2, 3, and 4.

The MT potential was constructed following the method suggested by Mattheiss,¹² by overlapping Dirac-Slater self-consistent relativistic atomic electron densities which were calculated separately, with the Slater $\rho^{1/3}$ approximation ($\alpha = 1$) for the exchange and correlation¹⁵ in the atomic as well as in the crystal potential.

The calculated ground-state configuration of the Ti atom, $3d^3 4s^1$, was used. The potential param-

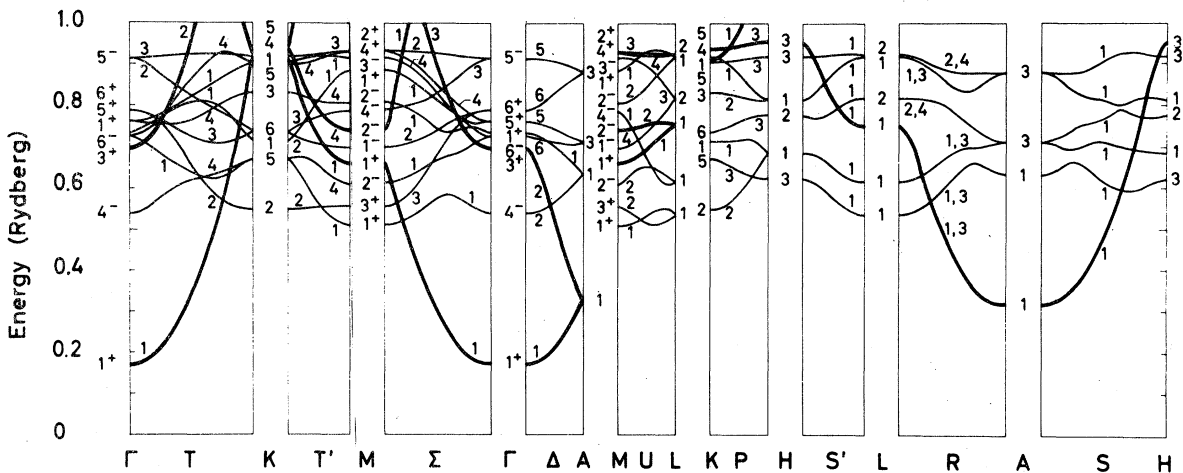


FIG. 2. Relativistic band structure of Ti ($c/a = 1.5873$) in the ASA, neglecting spin-orbit coupling and hybridization between the sp bands, indicated by thick lines, and the d bands.

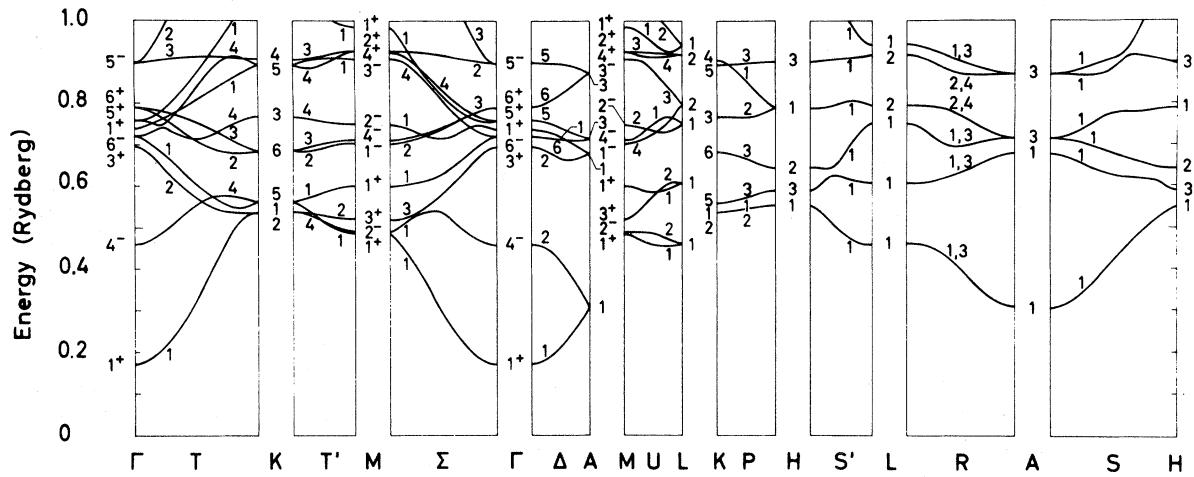


FIG. 3. Relativistic band structure of Ti neglecting spin-orbit coupling.

eters for this potential and with E_F chosen close to the estimated Fermi energy may be found in Table I. Together with the structure constants these potential parameters may be used to reproduce our energy bands.

The Fermi level, state density, and extremal Fermi-surface areas were computed automatically with a linear-interpolation technique employing tetrahedral microzones.¹⁶ The eigenvalues were calculated at 396 points in the irreducible zone, including points on the symmetry planes, thus dividing this wedge into 1500 tetrahedrons. The points were distributed on each of six equidistant planes perpendicular to the ΓA direction, with mesh planes parallel to the $\Gamma A L M$, $\Gamma A H K$, and $K H L M$ planes. The errors in the calculated extremal areas due to the linear interpolation can be estimated to be less than $\frac{1}{2}a^2 \approx 1$ MG, where a is the largest edge length in the tetrahedron.¹⁷ A

test calculation on⁴ Ru comparing the results for a 2541-point mesh with those for the 396-point mesh was in agreement with the estimate given above; moreover, the difference in Fermi energies for the two meshes was only 0.2 mRy. In Sec. III our results will be compared with those for different potentials obtained by the APW method. It has been shown by test calculations on Yb that, for the same potential, the linear MTO and relativistic APW methods give the same energy bands to within an rms deviation of 3 mRy.¹⁸

III. RESULTS

A. Energy bands

We shall discuss the energy bands of Ti in terms of the constituent sp and d bands and thereby emphasize its similarity to the other group-IV elements. However, in contrast to the discussion of

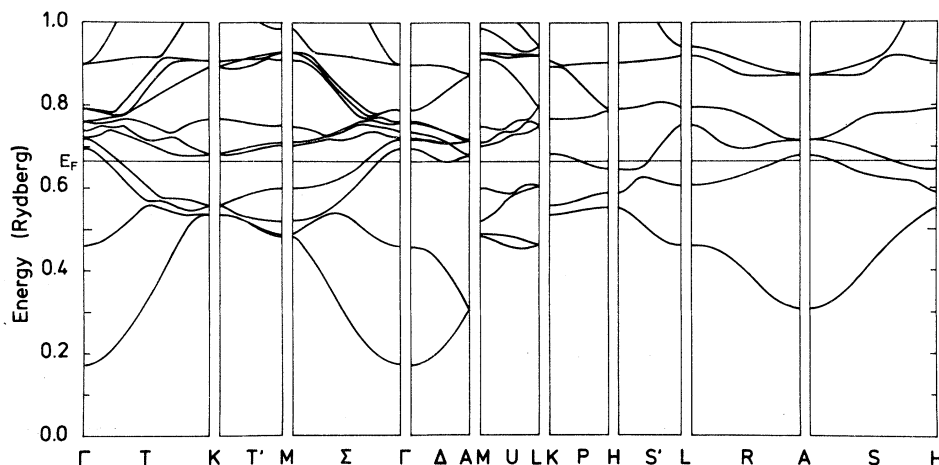


FIG. 4. Relativistic band structure of Ti.

TABLE I. Potential parameters from which the band structure of Ti was calculated.

	$E_v - V_{\text{MTZ}}$ (Ry)	$\omega(-l-1)$ (Ry)	$10S\Phi^2(-l-1, S)$ (Ry)	$\frac{\Phi(-l-1, S)}{\Phi(l, S)}$	$\langle \phi_{\nu}^2 \rangle^{-1/2}$ (Ry)	$\xi(D_{\nu})$ (Ry)	$\omega(D^I)$ (Ry)
<i>s</i>	0.600	-0.078	3.026	0.853	3.9
<i>p</i>	0.600	0.728	2.747	0.699	4.9	0.0075	-14.0
<i>d</i>	0.600	0.173	0.401	0.096	0.90	0.0011	-0.97

Os in JAM, we have included the relativistic Darwin and mass-velocity shifts throughout.

The Brillouin zone for the hcp structure is illustrated in Fig. 1. In Fig. 2 we show the relativistic energy bands of Ti along the symmetry lines of the zone in the ASA, neglecting spin-orbit coupling and also eliminating the hybridization between the *sp* and *d* bands by setting the nondiagonal structure constants involving $l=2$ equal to zero. The *d* bands bear a strong resemblance to the canonical *d* bands as may be seen for $c/a=1.633$ in Fig. 2 of JAM. They are located in energy by C_{ds} of Table II and scaled uniformly by the parameter μ_d . The nonuniform distortion represented by γ_d and $\langle \phi_{\nu d}^2 \rangle$ of Table I is small. The *sp* bands are much broader than the *d* bands and also about 30% broader than the free-electron bands, as may be seen from the mass parameters μ_s and μ_p of Table II.

The effect of hybridization between the *sp* and *d* bands may be appreciated by comparing Figs. 2 and 3, since all nondiagonal structure constants

are included in the latter. Moreover it may be seen that the correction term which is included in Fig. 3 results in small downward shifts near the top of the *d* bands of the nonhybridizing *d* levels. The hybridization has drastic effects on the *sp* bands, whose characteristic parabolic form only survives above and below the *d*-energy range. It also results in large shifts and changed connectivities of the *d*-bands. The two K_1 levels, which without hybridization are purely *p*- and *d*-like, repel each other and the lower of these becomes nearly degenerate with the K_2 level. The lowest band along the line *P*, from *K* to *H* therefore consists of the two almost degenerate P_1 and P_2 bands. The low energy of the purely *p*-like Γ_3^+ level results in strong hybridization of the two crossing Δ_2 bands. The uppermost of these is very important in determining the topology of the Fermi surface, which thus critically depends on the relative position of the *sp* and *d* bands. The relativistic Ti bands including spin-orbit coupling are shown

TABLE II. Potential parameters for Ti and Zr calculated as described in the text. The values under NR were calculated with the same potential construction, but omitting the relativistic effects in the solid. The values under NRA were calculated with the omission of all relativistic effects, both in the atom and the solid.

Titanium ($S=3.052$ a.u.)					
Configura- tion	$3d^34s^1$ ^a	$3d^24s^2$	$3d^24s^2$ (NR)	$3d^24s^2$ (NRA)	$3d^24s^2$ (NR) ^b
C_{ps}	7.36	7.29	7.23	7.22	7.22
C_{ds}	2.28	1.37	1.26	1.17	-0.99
μ_s	0.71	0.72	0.71	0.71	0.74
μ_p	0.83	0.84	0.84	0.84	0.81
μ_d	6.0	7.2	7.2	7.4	12.0
ξ_d (mRy)	1.5	1.7	0.0	0.0	0.0
Zirconium ($S=3.347$ a.u.)					
Configura- tion	$4d^35s^1$ ^c	$4d^25s^2$	$4d^25s^2$ (NR)	$4d^25s^2$ (NRA)	$4d^25s^2$ (NR) ^d
C_{ps}	8.61	8.56	8.36	8.28	8.89
C_{ds}	2.79	2.46	2.00	1.78	2.59
μ_s	0.69	0.69	0.67	0.68	0.69
μ_p	0.77	0.77	0.77	0.77	0.76
μ_d	3.6	3.8	3.8	4.0	3.7
ξ_d (mRy)	4.4	4.7	0.0	0.0	0.0

^aPresent calculation.

^bReference 5.

^cReference 4.

^dReference 20.

in Fig. 4. All bands are fourfold degenerate (including spin) along the line R , joining A and L but away from this line on the hexagonal face the spin-orbit coupling lifts this degeneracy. Similarly the second and third bands along the line P consist of two sets of spin-orbit split bands; however due to the extremely small spin-orbit coupling parameter (~ 1.5 mRy) these splittings are not apparent on the figure. We shall demonstrate below how \mathbf{k} -space orbits in Ti intersecting the hexagonal face and near the line P are mixed due to magnetic breakdown of these small spin-orbit split levels.

Our Ti bands are very similar to JAM's results for Zr and Hf, with the general trend that the d bands rise and broaden relative to the sp bands as we go from Ti to Hf, due to the increased influence of the relativistic effects. This may be seen by comparing our potential parameters in Table II with those in Table II of JAM.

In order to elucidate the difference between our bands and those of Hygh and Welch, we have calculated the potential parameters for the potential listed by HW(I), which was constructed in the same way as our potential, but employing the $3d^2 4s^2$ configuration for the relativistic atomic electron densities of Liberman *et al.*¹⁹ These parameters may be found in the last column of Table II together with the parameters used in the present calculation and the relativistic, the semi-nonrelativistic (NR) and fully-nonrelativistic (NR A) parameters, all with the $3d^2 4s^2$ configuration. As expected, the relativistic effects in Ti are small, but not negligible. In the lower half of Table II the equivalent set of parameters are listed for Zr. The last column was found from the potential given by Loucks²⁰ who also used Mattheiss's potential construction and the relativistic electron densities of Liberman *et al.*¹⁹ The NR potential parameters for Ti as well as Zr were obtained with the same programs as the relativistic parameters but the velocity of light was set to infinity in the logarithmic derivative calculation, and the NR A parameters were obtained in the same way by omitting the relativistic effects in the atomic calculation also. It should be noted that Hygh and Welch and Loucks used a semi-nonrelativistic (NR) potential.

As will be seen from Table II a change of configuration from s^1 to s^2 mainly results in lower and narrower d bands, and this effect is more pronounced for the $3d$ element than for the $4d$ element. Removing the relativistic terms has the same general effect on the bands but here the changes are greater for the heavier Zr than for Ti, as expected. The relativistic shifts and the spin-orbit parameter ξ_d , calculated at the center of the d band, are roughly three times greater for Zr than for Ti, as was also found for Os($5d$) compared with Ru($4d$).⁴

Whereas the position and width of Loucks's bands

are in reasonable agreement with our calculations, the d bands of HW(I) lie about 250 mRy lower and are about a factor of 2 narrower than ours. The electronic structures calculated by WH(II) with a self-consistent potential (but with non-self-consistent core densities) and $\alpha = \frac{3}{4}$ and by WH(III) using the s^1 configuration in the atom were essentially the same as that of HW(I). Mattheiss's⁹ APW bands calculated with a MT potential constructed from a nonrelativistic Hartree-Fock self-consistent atomic potential with the $3d^3 4s^1$ configuration is in good overall agreement with our bands.

These comparisons of potential parameters for Zr and Ti seem to indicate that the method of potential construction used by Hygh and Welch differs from that which we have adopted in a way which is not fully apparent from their papers.

B. State density

The density of states is shown in Fig. 5. The Fermi energy E_F and the state density at E_F , $N(E_F)$, found from this plot are given in Table III, together with the value of the Fermi surface parameter

$$s_d(E_F) \equiv 10[D_d(E_F) + 3]/[D_d(E_F) - 2].$$

The approximate number of d electrons n_d is obtained by integrating the canonical density of states up to $s_d(E_F)$, i.e., from the canonical $n_d(s)$,²¹ and is also given in the table.

A comparison of our n_d value for Ti with those found for Zr and⁴ Hf shows that the d -band occupancy increases from Ti to Zr and decreases from Zr to Hf, resulting in nearly the same number of d electrons in Ti and Hf. This is consistent with the energy bands, as may be seen by comparing the potential parameters for these three metals. The d bands rise and broaden from Ti to Hf but the band width of Ti is so small that the position of the bottom of the d bands is higher relative to the sp bands than in Zr and Hf.

The state densities of Ti, Zr, and Hf are very similar, with three characteristic hybridization energy gaps. In all three metals the Fermi energy falls on the high-energy side of the deepest central gap.

The ratio between the electronic heat capacity as determined from $N(E_F)$ and the experimental value²² represents our estimate of the phonon enhancement of $N(E_F)$. It seems to be somewhat too high compared with the value deduced by McMillan²³ from the superconducting properties. A larger value of $N(E_F)$ could be obtained by a lowering of the d bands relative to the sp bands which would result in a somewhat smaller decrease in E_F and therefore a relative increase in the Fermi level with respect to the rapid rise in $N(E)$ illustrated in Fig. 5. We can obtain McMillan's value

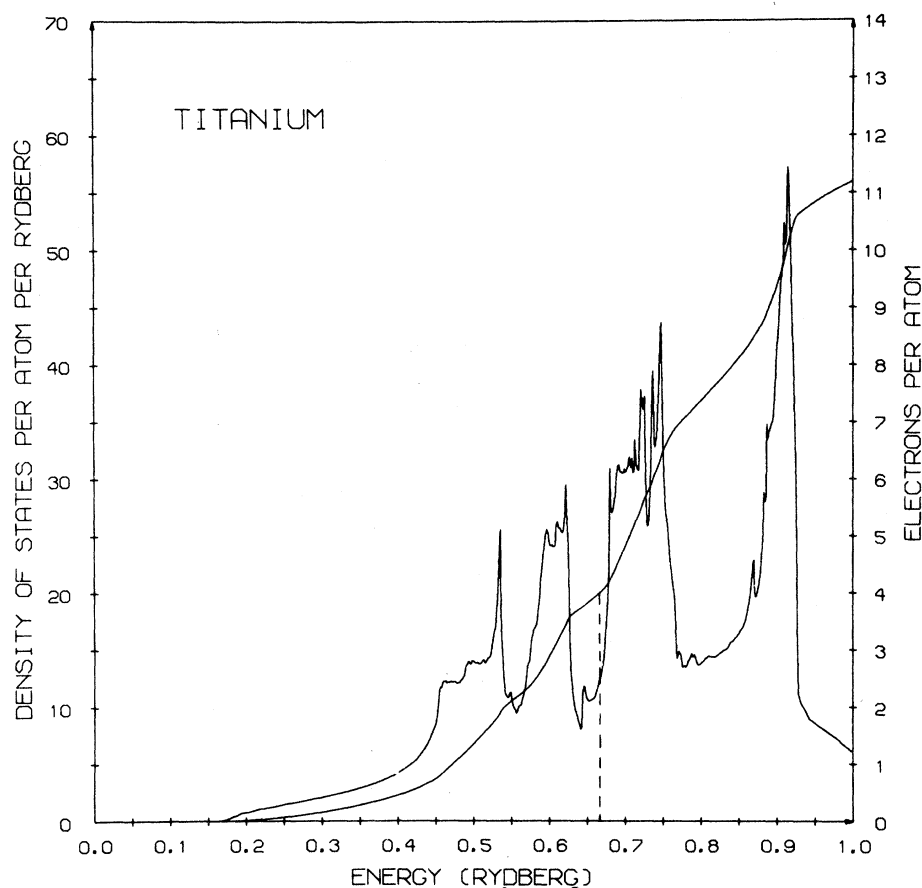


FIG. 5. Density of states and number of states of Ti. The Fermi energy is indicated by the dashed line.

of the enhancement factor by increasing E_F by only 4.6 mRy. This indication that the d bands lie slightly too high is in agreement with the comparison of our Fermi surface with the dHvA measurements discussed below.

C. Fermi surface

From the energy eigenvalues at the mesh points and Fermi energy given in Table III the Fermi-surface sections in Fig. 6 were calculated, assuming linear variation of the energy between neighboring mesh points.

With a notation equivalent to that used by JAM, in which the position of the center of the surface (or the open direction of an open surface), the band in which it lies and its electron or hole character are specified, the Fermi surface comprises one open $\Gamma A4h$ surface and four closed surfaces $\Gamma 3h$, $A3h$, $H5e$, and $H6e$. This surface is topologically equivalent to those of Zr and Hf calculated by JAM, but with the important difference that the open $\Gamma A3h$ surface found by them is disconnected near A in Ti.

The Fermi surface of Ti has been studied through the dHvA effect by Kamm and Anderson.²

Although their results are preliminary, they are sufficiently complete to compare with our Fermi surface model, with which they are in good agreement. The theoretical and experimental extremal areas and effective masses are given in Table IV for the principal symmetry directions. The Greek letters correspond to the notation used by Kamm and Anderson.

We associate the approximately isotropic α branch with the $\Gamma 3h$ surface, although our values

TABLE III. Fermi-surface parameters and electronic heat capacities.

$E_F - V_{MTZ}$ (Ry)	0.667
$s_d(E_F)$	-5.57
n (states/atom)	4.0
n_d (states/atom)	2.47
$N(E_F)$ (states/atom Ry)	12.4
γ_{theor} (mJ/mol °K ²)	2.15
γ_{expt} (mJ/mole °K ²) ^a	3.32
$\gamma_{\text{expt}}/\gamma_{\text{theor}}$	1.54
Theoretical enhancement ^b	1.38

^aReference 22.

^bReference 23.

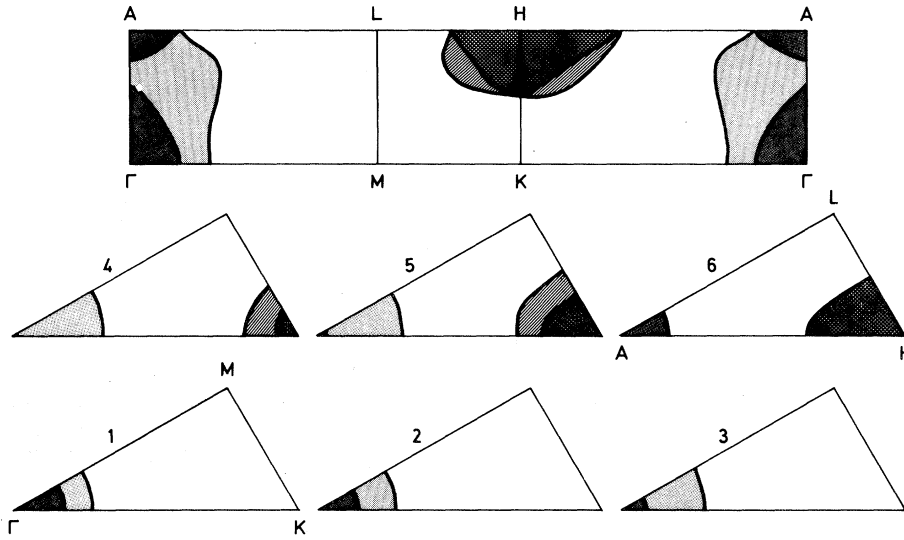


FIG. 6. Sections of the Ti Fermi surface in the irreducible Brillouin zone. At the top are shown intersections with the faces of the irreducible zone, while six equidistant sections normal to [0001] are depicted at the bottom. Third- and fourth-zone hole regions are shaded; fifth- and sixth-zone regions are shown by diagonal lines and cross hatching.

are somewhat larger than those observed. However, because of the flatness of the third band an upwards shift of E_F of only 6 mRy would bring the theoretical and experimental values into coincidence. The β orbit is associated with the maximum area on the nearly cylindrical $\Gamma A4h$ surface and for this sheet an upwards shift of only 4 mRy in E_F is required to bring it into agreement with the observed value.

As suggested by Kamm and Anderson, magnetic breakdown is essential for the interpretation of the five ϵ branches, which are nearly equally spaced and nearly independent of angle. As discussed above, magnetic breakdown is very likely to occur even for moderate magnetic fields between the fifth and sixth bands at the hexagonal face of the Brillouin zone and near the line P , connecting H and K . Consequently the ϵ branches are associated with the coupled orbits of the two H -centered electron surfaces and these are shown for the $[10\bar{1}0]$ direction in Fig. 7. Owing to the mirror symmetry with respect to the hexagonal face of the zone, the differences between ϵ_2 and ϵ_1 and between ϵ_5 and ϵ_4 , are the same and measured to be 3.3 MG. Similarly the differences between ϵ_3 and ϵ_2 and between ϵ_4 and ϵ_3 are measured to be 2.7 MG. Our values are 4.0 and 3.8 MG, respectively. The magnitude of these differences in the $[11\bar{2}0]$ direction are all equal, since then the $\Gamma A H K$ plane is also a mirror plane for the two sheets. This difference is measured to be 3.3 MG and our calculations give a value of 4.1 MG.

As the magnetic field is rotated out of the basal plane the ϵ_2 and ϵ_4 branches disappear. This can be explained from the approximate expression for the tunneling probability (in SI units) between two orbits derived by Chambers²⁴:

$$P = \exp \left[-\frac{\pi \hbar}{2eH} \left(\frac{k_g^3}{1/a + 1/b} \right)^{1/2} \right],$$

where k_g is the size of the \bar{k} -space gap between the orbits and a and b are the radii of curvature of the orbits at the points where the breakdown occurs. As may be seen in Fig. 6, k_g increases as the

TABLE IV. Fermi-surface areas and cyclotron masses for Ti. The experimental results are taken from Ref. 2.

Titanium						
Direction		Extremal areas (MG)		Cyclotron masses (m/m_0)		Ratio
		Theor.	Expt.	Theor.	Expt.	
$A3h$	$[10\bar{1}0]$	10.8		0.68		
	$[11\bar{2}0]$	11.2		0.67		
	$[0001]$	20.2		1.59		
$\Gamma 3h$	$[10\bar{1}0] \alpha$	27.5	17.5	1.43	1.7	1.2
	$[11\bar{2}0] \alpha$	28.0	17.5	1.54	1.55	1.0
	$[0001] \alpha$	21.2	15.7	0.67	1.0	1.5
$\Gamma A4h$	$[0001]$	51.5		1.21		
	$[0001] \beta$	68.0	60.5	1.68	2.0	1.2
	$[0001]$	20.3		1.59		
$H6e$	$[10\bar{1}0] \epsilon_1$	33.5	37.0	1.66	2.7	1.6
$H56e$	$[10\bar{1}0] \epsilon_2$	37.4	40.3	1.65		
	$[10\bar{1}0] \epsilon_3$	41.3	43.0	1.80	2.7	1.5
	$[10\bar{1}0] \epsilon_4$	45.1	45.7	1.96		
$H5e$	$[10\bar{1}0] \epsilon_5$	49.1	49.0	1.95		
$H6e$	$[11\bar{2}0] \epsilon_1$	32.5	36.0	1.66	2.8	1.7
$H56e$	$[11\bar{2}0] \epsilon_2$	36.6	39.3	1.68		
	$[11\bar{2}0] \epsilon_3$	40.7	42.6	1.70	2.6	1.5
	$[11\bar{2}0] \epsilon_4$	44.8	45.8	1.72		
$H5e$	$[11\bar{2}0] \epsilon_5$	48.9	49.1	1.74	2.7	1.6
$H5e$	$[0001]$	54.2		1.80		
	$[0001]$	55.9		1.55		
$H6e$	$[0001]$	53.0		1.77		

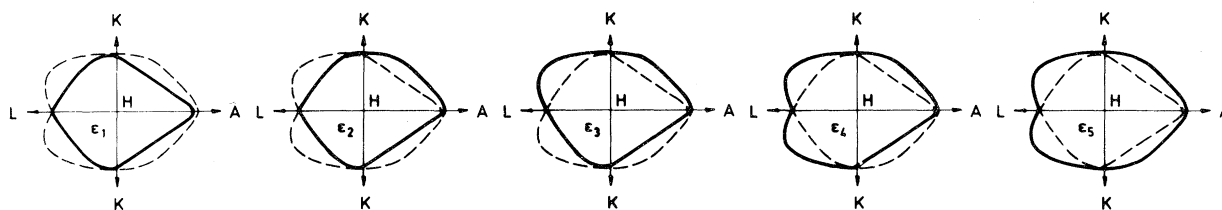


FIG. 7. Breakdown orbits ϵ_1 to ϵ_5 with the magnetic field in the $[10\bar{1}0]$ direction.

orbit is rotated away from the line P , resulting in a smaller tunneling probability. ϵ_1 , ϵ_3 , and ϵ_5 are also observed to disappear, but this occurs for directions further away from the basal plane. It should however be possible to detect these branches all the way to the c direction, since ϵ_1 and ϵ_5 are pure $H6e$ and $H5e$ orbits and ϵ_3 results from breakdown on the hexagonal face only. Our ϵ branches are too small by an amount corresponding to an upwards shift of E_F of only about 2 mRy.

It is interesting to compare these results for Ti with the very similar electron surfaces in Zr and Hf. The spin-orbit coupling is approximately three times larger for Zr than for Ti, so for the very flat bands in the P direction, the \bar{k} -space gap is greater in Zr and consequently the probability of magnetic breakdown is smaller. At the hexagonal face the bands are sufficiently curved that the possibility of magnetic breakdown still exists and three orbits η , δ , and ζ corresponding to ϵ_1 , ϵ_3 , and ϵ_5 in Ti are observed in the dHvA results of Everett.³ In Hf the spin-orbit coupling is so large that magnetic breakdown between the two electron sheets will only occur for very large magnetic fields, even on the hexagonal face.

In summary, the hole surfaces are calculated to be somewhat larger and the electron surfaces somewhat smaller than observed. Since the Fermi level in the transition metals is determined principally by the position of the d bands, a shift in C_{ds} is accompanied by a shift in E_F which is of the same sign and slightly smaller. Because of the flatness of the d bands, a relative decrease in their energy of only about 10 mRy is required to bring

both hole and electron areas into coincidence with the experimental values. As mentioned above, such a shift seems also to be consistent with the heat capacity results.

IV. CONCLUSION

In this paper we have reported the results of a calculation of the electronic structure of hcp Ti by the linear MTO method. The agreement between the calculated Fermi surface and dHvA measurements is very good and in the interpretation of these results it has been demonstrated that, as in other hcp metals, magnetic breakdown is important. The one-electron potential was approximated by a muffin-tin potential constructed in the standard way by superposing relativistic atomic electron densities, with exchange and correlation included in the Slater $\rho^{1/3}$ approximation. It has been demonstrated for the first time for a $3d$ transition metal that such a potential gives the relative position of the s , p , and d bands to within about 10 mRy and therefore a Fermi surface which is in good quantitative agreement with experiment. When further dHvA results become available, it will be possible to make a more detailed comparison between our calculations and the experimentally determined Fermi surface.

ACKNOWLEDGMENTS

The author wishes to express his sincere gratitude to Dr. O. Krogh Anderson and Professor A. R. Mackintosh for many fruitful discussions during the course of this research.

¹O. K. Andersen, Phys. Rev. B 2, 883 (1970); D. D. Koelling, F. M. Mueller, and A. J. Arko, *ibid.* 10, 4889 (1974); N. Egede Christensen and B. Feuerbacher, *ibid.* 10, 2349 (1974), L. F. Mattheiss, *ibid.* 1, 373 (1970).

²G. N. Kamm and J. R. Anderson, *Low Temperature Physics* (Plenum, New York, 1974), Vol. 4.

³P. M. Everett, Phys. Rev. B 6, 3559 (1972).

⁴O. Jepsen, O. K. Andersen, and A. R. Mackintosh, Phys. Rev. B 12, 3084 (1975).

⁵E. H. Hygh and R. M. Welch, Phys. Rev. B 1, 2424

(1970).

⁶R. M. Welch and E. H. Hygh, Phys. Rev. B 4, 4261 (1971).

⁷R. M. Welch and E. H. Hygh, Phys. Rev. B 9, 1993 (1974).

⁸S. L. Altmann and N. V. Cohan, Proc. Phys. Soc. 71, 383 (1958).

⁹L. F. Mattheiss, Phys. Rev. 134, A970 (1964).

¹⁰S. L. Altmann and C. J. Bradley, Proc. Phys. Soc. 92, 764 (1967).

¹¹O. K. Andersen, Phys. Rev. B 12, 3060 (1975).

- ¹²L. F. Mattheiss, Phys. Rev. 133, A1399 (1964).
- ¹³O. K. Andersen, Solid State Commun. 13, 133 (1973).
- ¹⁴W. E. Pearson, *A Handbook of Lattice Spacings and Structures of Metals and Alloys* (Pergamon, New York, 1958).
- ¹⁵J. C. Slater, Phys. Rev. 81, 385 (1951).
- ¹⁶O. Jepsen and O. K. Andersen, Solid State Commun. 9, 1763 (1971).
- ¹⁷O. Jepsen, thesis (Technical University of Denmark, 1971) (unpublished).
- ¹⁸O. Jepsen and O. K. Andersen (unpublished).
- ¹⁹D. Liberman, J. T. Waber, and Don T. Cromer, Phys. Rev. 137 A27 (1965).
- ²⁰T. L. Loucks, Phys. Rev. 159, 544 (1967).
- ²¹O. K. Andersen and O. Jepsen (unpublished).
- ²²J. G. Daunt, *Progress in Low Temperature Physics* (North-Holland, Amsterdam, 1955).
- ²³W. L. McMillan, Phys. Rev. 167, 331 (1968).
- ²⁴R. G. Chambers, Proc. Phys. Soc. 88, 701 (1966).